

High-Throughput Nanofabrication of Metasurfaces with Polarization-Dependent Response

Cristiano Matricardi, Juan Luis Garcia-Pomar, Pau Molet, Luis Alberto Pérez, Maria Isabel Alonso, Mariano Campoy-Quiles, and Agustín Mihi*

Metal nanostructures offer exciting ways to manage light at the nanoscale exploited in fields such as imaging, sensing, energy conversion, and information processing. The optical response of the metallic architectures can be engineered to exhibit photonic properties that span from plasmon resonances to more complex phenomena such as negative refractive index, optical chirality, artificial magnetism, and more. However, the latter optical properties are only observed in intricate architectures, which are highly demanding in terms of nanofabrication and hence less scalable and far away from device implementation. Here, a series of metasurfaces covering centimeter areas and operating in the visible spectrum are presented, which are produced from the combination of nanoimprinting lithography and oblique angle metal evaporation. The potential of this scalable approach is illustrated by easily fabricating metasurfaces engineered to exhibit artificial optical magnetism, tunable linear polarization dependent response, chirality with *g*-factor of 0.2, and photoluminescence enhancement of 20 times over a 9 mm² area.

and induced transparency.^[13,14] In these geometries, the excitation of antisymmetric plasmonic resonances can result in magnetism at optical frequencies, a key property for magnetic and left-handed components for visible optics. However, achieving a metamaterial composed of split ring resonators is not an easy task and the fabrication of such structures relies heavily on conventional low throughput lithographic processes. Another exciting optical property is chirality, which in plasmonics enables enantiomer detection and separation.^[15,16] Despite the great interest to obtain chiral nanostructures, achieving this particular lack of symmetry in a scalable fashion remains a challenge.


In general, plasmonic architectures are produced by focused electron or ion beam lithography, techniques that provide high resolution and versatility but that are difficult to scale up.

1. Introduction

Metal nanostructures can be engineered to sustain a wide variety of resonances. From the simplest localized surface plasmon resonance observed in a metal colloid,^[1] until the more complex magnetic and electric resonances sustained by metamaterials.^[2,3] The diverse optical properties sustained by nanostructured metals have led to advances in biosensing,^[4] photovoltaics,^[5,6] imaging,^[7] and lighting.^[8] However, complex optical phenomena such as chirality, negative refraction, and optical magnetism are typically sustained by precisely engineered nanostructures with broken symmetries whose cumbersome fabrication process is far from scalable. For instance, asymmetrically split rings exhibit unusually strong high-Q resonances^[9] with multiple uses in sensing,^[10] lasing,^[11,12]

On the other side of the spectrum there are fabrication techniques compatible with mass production but more restrictive in terms of the produced features such as nanosphere lithography (NSL),^[17] interference lithography (IL),^[18] and nanoimprinting lithography (NIL).^[19–22] These lithographies, however, tend to produce symmetric periodic nanostructures which limit the number of optical properties accessible. One way to gain access to polarization-dependent response is by breaking the symmetry of the original array. This can be achieved simply by tilting the sample at the metallization stage, opening up a plethora of possibilities. The combination of NSL with oblique angle deposition (OAD) has led to a variety of asymmetric plasmonic nanostructures^[23,24] from split ring resonators^[25] to chiral nanostructures^[26,27] and complex 3D plasmonic nanostructures.^[28,29] However, in the case of NSL, the microspheres tend to self-assemble almost exclusively into hexagonal arrays whose large-scale homogeneity is severely affected by the presence of cracks and defects of the final assembly, which in turn deteriorates the overall optical response and broadens the plasmonic resonances. Alternatively, NIL is the technique of preference for the upscaling of nanostructures with excellent quality, it is roll-to-roll compatible and it has an excellent resolution without requiring complex optical setups.^[30,31] In NIL, prepatterned elastomeric molds are used as printing stamps in which the geometry, feature depth, and lattice parameter can be varied by changing the original master. These nanostructures combined with OAD can result in a rich variety of novel asymmetric plasmonic architectures; however, the versatility and potential

C. Matricardi, Dr. J. L. Garcia-Pomar, P. Molet, Dr. L. A. Pérez, Dr. M. I. Alonso, Dr. M. Campoy-Quiles, Dr. A. Mihi
Instituto de Ciencia de Materiales de Barcelona (ICMAB-CSIC)
Campus UAB, Bellaterra 08193, Spain
E-mail: amih@icmab.es

 The ORCID identification number(s) for the author(s) of this article can be found under <https://doi.org/10.1002/adom.202000786>.

© 2020 The Authors. Published by WILEY-VCH Verlag GmbH & Co. KGaA, Weinheim. This is an open access article under the terms of the Creative Commons Attribution-NonCommercial License, which permits use, distribution and reproduction in any medium, provided the original work is properly cited and is not used for commercial purposes.

DOI: 10.1002/adom.202000786

of this approach has only been hinted at by a few reports in the literature, which led to chiral structures and surface-enhanced Raman spectroscopy (SERS) substrates.^[32,33]

In this work, we demonstrate a scalable and simple fabrication procedure that is used to produce large-area and homogeneous metasurfaces exhibiting complex optical properties. We combine NIL with oblique angle metallization to produce 2D arrays composed of unit cells with different degrees of asymmetry, which confer the metasurface with linear polarization dependent response, chirality, optical magnetism, or strong near-field enhancement. We first study how the degeneracy of the resonances sustained by a square hole array is broken when we evaporate a metal over a tilted sample. This symmetry breaking can be pushed further with subsequent metal evaporations leading to structural color architectures, magnetic resonances, and ultimately chiral plasmonic nanostructures. Finally, we show metasurfaces with varying depth of the nanoimprinted features, effectively creating an array of nanogaps with intense near-field effect. We used this latter system to illustrate the homogeneity of our metasurfaces by measuring a 20-fold photoluminescence enhancement averaged over a $3 \times 3 \text{ mm}^2$ area. We illustrate here a few of the many architectures and properties that can be achieved with this simple and versatile approach, however we believe that the combination of NIL and OAD paves the way toward the exploitation of these singular optical phenomena in real devices.

2. High-Throughput Fabrication of Tunable Asymmetric Nanostructures

Nanoimprinting lithography has many advantages; for instance, the great variety of nanoimprinted structures available, from hole arrays to pillars or pyramids, that can also be arranged into square, triangular, or other lattices.^[18] In the present work, we focus in square arrays of holes with varying depth and lattice parameter.

The fabrication of the nanostructures begins with the nanoimprinting of a photonic crystal nanostructure in a 600 nm thick epoxy film (SU8 2000.5, Microchem) using a prepatterned polydimethylsiloxane mold (PDMS). Pressing the stamp onto the substrate at a temperature over the glass transition of the resist is enough to replicate the negative features on the film (Figure S1, Supporting Information and Experimental Section). After demolding, the films underwent UV curing and annealing on a hot plate (150 °C, 30 min). The samples are then placed on a custom-made evaporator holder featuring 0°, 20°, and 45° tilt angle θ , followed by thermal evaporation of 75 nm of Ag (Figure 1a). During the oblique metal evaporation, certain regions of the nanostructure remain shadowed thus progressively reducing the symmetry of the unit cell. Full details on the evaporation conditions and alignment with respect to the thermal source are given in Figure S2 (Supporting Information).

The resulting plasmonic architectures obtained by the oblique metal deposition at different angles over a nanoimprinted square array of holes with 350 nm depth, 300 nm diameter, and lattice parameter $L = 400$ and 500 nm,

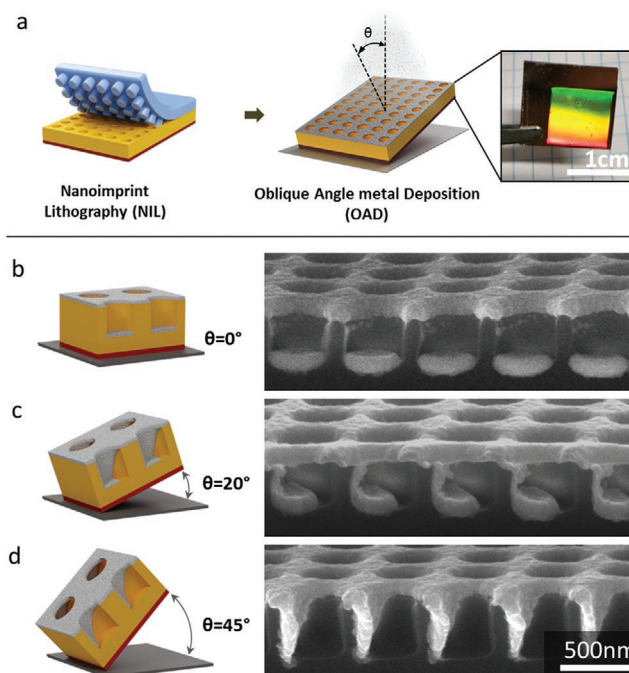


Figure 1. Schematic representation of the fabrication process leading to asymmetric nanostructures. a) The samples are fabricated by NIL followed by thermal evaporation of Ag at different tilt angles. b–d) Sketch and SEM image of the plasmonic architectures fabricated by 0°, 20°, and 45° tilt Ag evaporation (75 nm) over a square array of holes with lattice parameter 500 nm and hole diameter 300 nm.

respectively, are summarized in Figure 1. The progressive shadowing angle leads to the formation of different asymmetric shapes within the holes, going from disconnected disks (0° tilt) to spoon-like (20° tilt) up to sharp wedges (45° tilt).

In order to characterize the effect of the OAD on the original structure, we collected the specular reflectance from the samples under linearly polarized light (Figure 2). Under normal evaporation conditions (0° tilt angle), the reflectivity in both linear polarizations shows only slight differences accounting for the inherent asymmetries of the thermal evaporation setup. However, as we increase the tilting angle there is a breaking of the mode degeneracy for each linear polarization, accentuated as we increase the tilt angle from 0° to 45°. The splitting of the resonances for each polarization is observed in all the lattice parameters studied ($L = 400$, 500, and 600 nm, Figure S3, Supporting Information) although larger lattice parameters demand higher tilt angles to obtain a clear splitting (Figure 2a,b). The lattice parameter of the fabricated photonic crystal also determines the spectral position of the shifted resonances, in the studied cases being at 550–700 nm range for $L = 400$ nm (Figure 2a) and at the 700–850 nm range for $L = 500$ nm samples (Figure 2b). Therefore, our system also allows an easy tuning of the spectral position of the shifting resonances by changing its geometrical parameters.

The tilted metal evaporation on the square array breaks the symmetry of the unit cell and produces the excitation of specific plasmonic resonances for each linear polarization. A more dramatic effect on the optical properties can be achieved by carrying out a second oblique metal evaporation on the

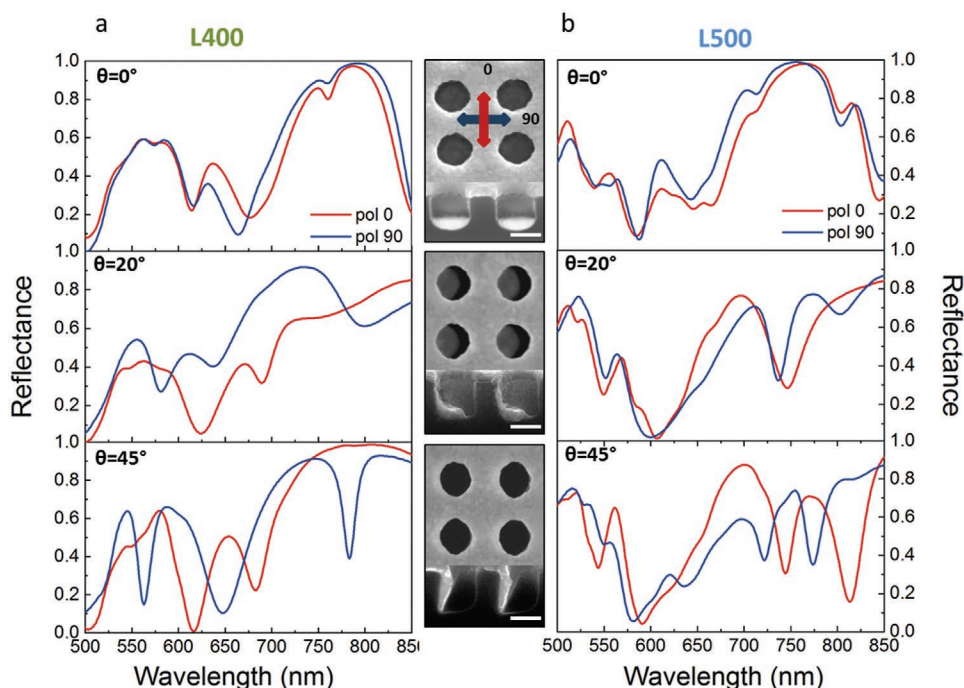


Figure 2. Optical characterization of asymmetric plasmonic crystals (square array of holes with diameter 300 nm and depth 350 nm) with lattice parameter a) 400 nm and b) 500 nm, for three different tilt angles (0° , 20° , and 45°) of Ag evaporation (75 nm). The linearly polarized reflectance spectra were taken along the two main crystal directions of the nanostructure, labeled as *pol 0* (red) and *pol 90* (blue). The samples were coated with 75 nm of Ag and showed negligible transmission. The middle column shows SEM images (top and cross section) from the 500 nm lattice parameter metasurface inspected in each case. Scale bars are 250 nm.

sample (Figure 3). In particular, the sample with lattice parameter 500 nm and metal coated at 45° tilt (shown in Figure 2b, $\theta = 45^\circ$) was in-plane-rotated by 180° and coated again with 75 nm of silver at a 45° tilting angle. The resulting structure

(Figure 3a,b) consisting of two opposite silver wedges shows a redshift of the main resonance from 535 to 615 nm by changing the polarization of the incident light. A close inspection of the spatial distribution of the electromagnetic fields using finite

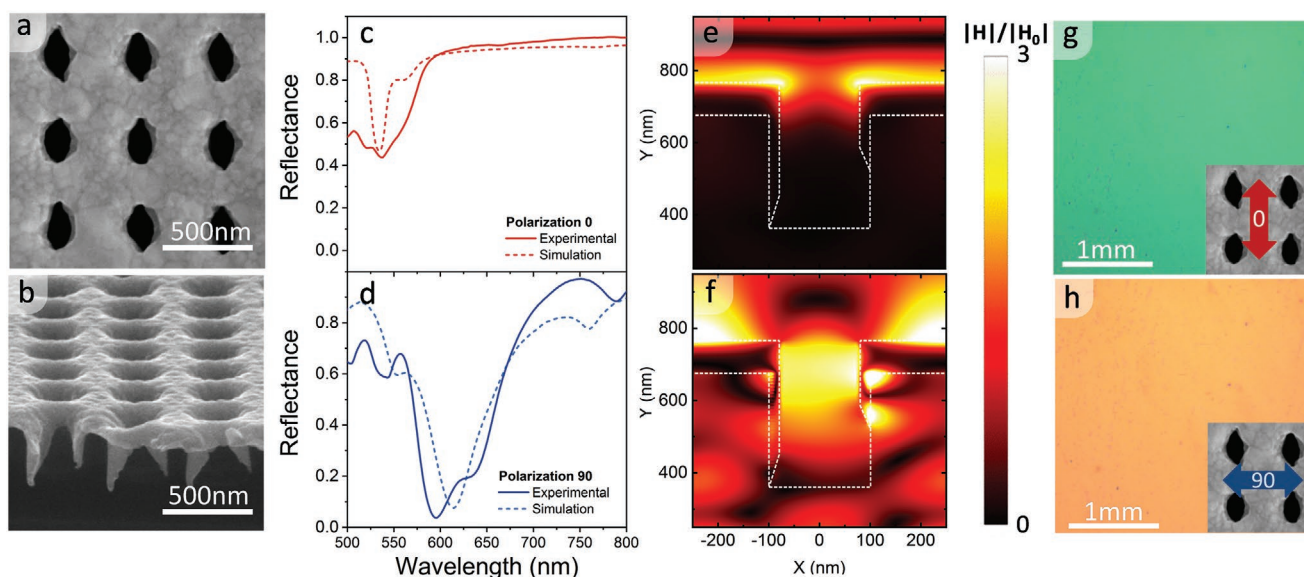


Figure 3. Asymmetric plasmonic crystal achieved after two consecutive 45° tilt metal evaporations. The original imprinted geometry consisted in a square array of holes with diameter 300 nm and depth 350 nm and lattice parameter 500 nm. The samples were coated with 50 nm of Ag with a tilting angle of 45° , rotated 180° in plane, and coated again at 45° . SEM images correspond to a) the top surface and b) cross section from the architecture. Linearly polarized reflectance spectra (experimental and simulated) relative to crystal lattice at c) 0° and d) 90° . FDTD simulations of the spatial distribution of the magnetic field at 615 nm for e) 0° and f) 90° linearly polarized light. Photographs obtained with an optical microscope of the sample under g) 0° and h) 90° linearly polarized light. The insets illustrate the plasmonic crystal geometry inspected in each case.

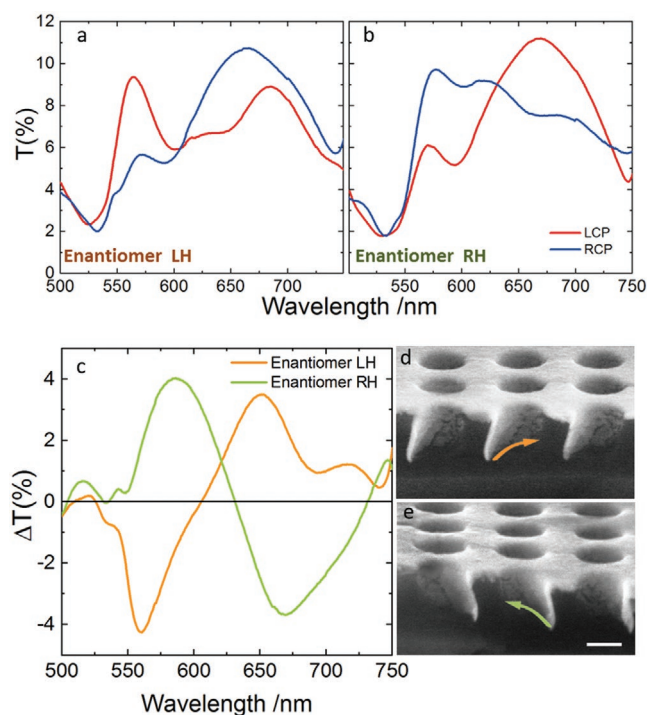


Figure 4. a,b) Transmission spectra of the chiral metasurfaces fabricated with three tilted evaporations of 20 nm of Ag at 45° under left and right-handed polarized light, respectively. c) Circular dichroism spectra for both enantiomers. SEM images and optical characterization of d) LH- and e) RH-plasmonic enantiomers fabricated by NIL and OAD.

difference time domain (FDTD) simulations reveals that incident light with polarization perpendicular to the wedges generates antisymmetric currents in the structure. These currents are responsible for the magnetic response in the cavity,^[34] while the other polarization does not induce any magnetic moment (Figure 3e,f). Furthermore, a polarization-dependent structural color change from green to orange is observed under inspection through an optical microscope with a linear polarizer (Figure 3g,h), in agreement with the polarized reflectance change. This type of architecture is therefore interesting as polarization-sensitive filters or to exploit artificial magnetism at visible frequencies.

In order to break further the symmetry of the original unit cell, we used three consecutive tilted evaporations at 45° with 25, 20, and 15 nm of Ag combined with in-plane rotations of the sample of 45° between evaporations. This process results in a chiral unit cell, since there are no mirror planes, in which the in-plane rotation direction of the sample between OADs determines the left- (LH) or right-handed (RH) orientation of the resulting enantiomer. The resulting two enantiomers fabricated with this process are illustrated in **Figure 4**. In the same way as with chiral molecules, the enantiomers of high-quality plasmonic chiral “molecules” present the same optical response and should be indistinguishable when measured with “traditional” transmitted linearly polarized light. We tested our chiral architectures with each of the three preferential polarization directions and both enantiomers presented similar optical responses,

proving their high quality and meaning that the structures fulfill the conditions for mirror images (see **Figure S4**, Supporting Information).

Next, we collected the transmittance from both enantiomers under circularly polarized light (**Figure 4a,b**) and calculated the difference in transmittance for each case (**Figure 4c**). It is worth noting that this simple fabrication procedure can result in chiral plasmonic structures with excellent values of circular dichroism (CD) at visible frequencies with a $\Delta T = 4\%$, whose optical response is uniform (**Figure S5**, Supporting Information) and can be easily engineered with the lattice parameter of the original array. In addition, we calculated a corresponding *g*-factor 0.21 at $\lambda = 588$ nm (**Figure S6**, Supporting Information), which is of great interest in the field, as illustrated by the many relevant applications of this property in chiral sensing^[35] or polarization-sensitive photochemistry.^[36] Full details on the optical characterization of these metasurfaces can be found in **Section S4** (Supporting Information).

Finally, we illustrate a metasurface displaying intense near-field regions that will be tested for their use in light emission. In the literature, nanometric gaps between metallic particles and antennas result in a strong field confinement that produced the greatest photoluminescence enhancement.^[37–39] Scaling up this geometry for its implementation in optoelectronic devices is quite challenging since it requires both great precision and uniformity over large areas to obtain a homogeneous response over the entire device. To produce an array of nanogaps fulfilling these requirements, we performed a single OAD over nanoimprinted samples with increasingly shallow features of 350, 120, 80, and 60 nm (see the Experimental Section). Metal coating of these nanostructures (tilt angle 45°, 75 nm of Ag) resulted in a series of arrays of nanogaps (**Figure 5**). While the samples with the original hole depth (350 nm) only present a wedge of silver (**Figure 5a**), samples with 120 and 80 nm deep holes feature homogeneous nanogap arrays of 80 and 30 nm, respectively (**Figure 5b,c**). Finally, in the 60 nm hole depth samples no gap is appreciated (**Figure 5d**). The metasurfaces with the 80 and 30 nm nanogaps show a resonance in the 750–850 nm range when impinging with a 90° linearly polarized light which is not present in the other two structures.

The performance of these nanogap metasurfaces for surface-enhanced light emission was tested by coating the samples with an organic dye. In particular, a mixture of Atto 655 dye (3×10^{-5} M) in a matrix of polyvinyl alcohol (PVA) was spin-coated on top of the samples producing a homogenous film of 250 nm thickness (**Figure S7**, Supporting Information). Embedding the molecular dye in a polymer matrix increases its stability while decreasing the intermolecular quenching. The PL measurements were excited with linearly polarized light and detected using a polarization analyzer set in parallel configuration. For these measurements, we chose to maintain the fixed alignment of the setup and rotate the sample at 0° or 90° to study the effect of the polarization on the PL spectra (**Figure S8**, Supporting Information). Upon excitation with a 633 nm linearly polarized laser light, the photoluminescence (PL) from the samples was found homogeneous throughout the inspected areas with a higher signal for the samples with the 30 nm gap width, with a maximum at 750 nm (**Figure 6b–d**). The averaged PL spectra for each linear polarization are shown in **Figure 6e,f**, where the

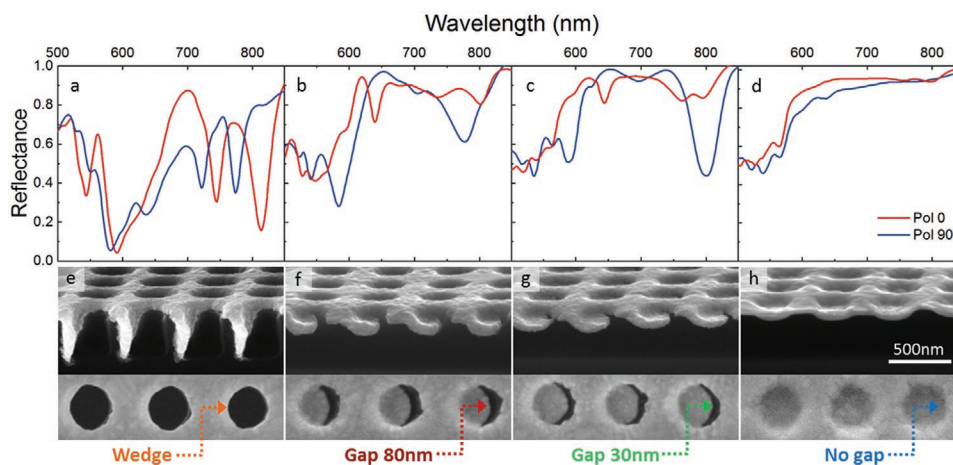


Figure 5. Optical properties and SEM images of plasmonic structures fabricated by tilted metal evaporation on NIL samples with decreasing feature depth and fixed 500 nm lattice parameter, 45° tilt angle, and 75 nm thickness of Ag. Polarization-resolved reflectance of wedges and SEM images for samples with feature depth of a,e) 350 nm, b,f) 120 nm, c,g) 80 nm, and d,h) 60 nm. Scale bar is 500 nm.

spectra from the nanogap metasurfaces (solid lines) are compared with the signal acquired from a flat reference (dashed lines). In addition to the main emission peak of the dye at 685 nm, an intense emission peak at 750 nm appears for both samples with nanogaps, being more intense in the case of the 30 nm gap array. The different PL intensity of the emitted light for both polarizations, suggests a polarization-selective interaction between the localized electric field and the photoluminescence.

The PL enhancement (PLE) calculated from the ratio between the signal measured from the plasmonic structure and that from a flat silver reference is depicted in **Figure 7a,c** (dashed lines). More than a 20-fold enhancement in photoluminescence averaged over the 3×3 mm² area was found for the sample composed of 30 nm gaps for the polarization orthogonal to the gap opening. It is worth noting that the PL enhancement was homogeneous for the entire area inspected proving the validity of this approach to achieve samples with homogeneous response over large areas.

In order to gain insight in the physics behind the enhancement, we reproduced the experimental reflectance spectra of

the 30 nm nanogap metasurfaces for both polarizations using the finite difference time domain (FDTD) method (**Figure 7**). The lattice plasmon resonance appears for this geometry around 750 nm. These plasmon surface waves, which depend on the angle of incidence and lattice parameter (**Figures S9 and S10**, Supporting Information), are scattered by the nanogap creating a higher enhancement of the PL. Due to the asymmetry, the propagating plasmons interact with the nanogaps at different orientations, being responsible for the different PLE in each linear polarization. This effect is further corroborated by the calculation (FDTD) of the Purcell factor (PF) of a dipole, with a wavelength of 750 nm, located in the middle of the nanogap (see the Experimental Section) with parallel and perpendicular polarization. The Purcell factor describes the emission rate enhancement of an emitter inside a cavity or resonator, which is correlated to the PL enhancement shown in **Figure 7c**. In agreement with the experiment, a higher Purcell factor is calculated for polarization perpendicular to the nanogap, obtaining a value of PF = 34 versus a value of PF = 3 for a polarization parallel to the nanogap.

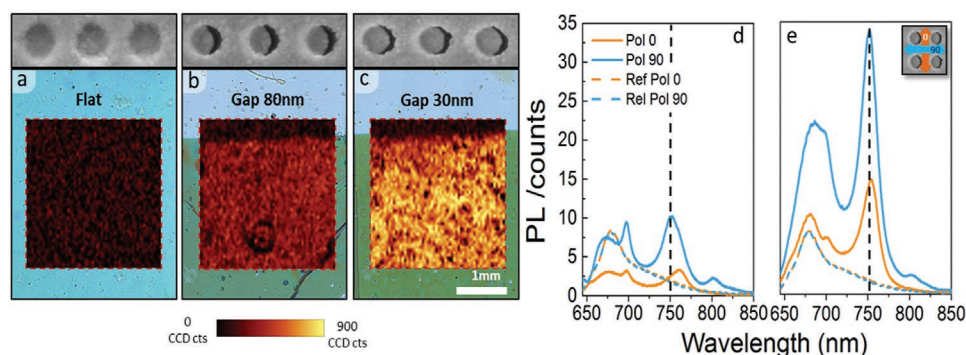


Figure 6. Photoluminescence from asymmetric plasmonic structures coated with a 250 nm thick layer of PVA/Atto 655. The signal was averaged over a 3×3 mm² area. a–c) PL images (90° linear polarization) of the 3×3 mm² inspected area at $\lambda = 750$ nm \pm 20 nm for the three different samples superimposed to the corresponding image of each sample. Averaged PL spectra for metasurfaces with d) 80 nm gap and e) 30 nm gap, for both linear polarizations versus PL measured for the flat reference (blue and orange dashed lines). Inset: SEM image of the corresponding geometry inspected.

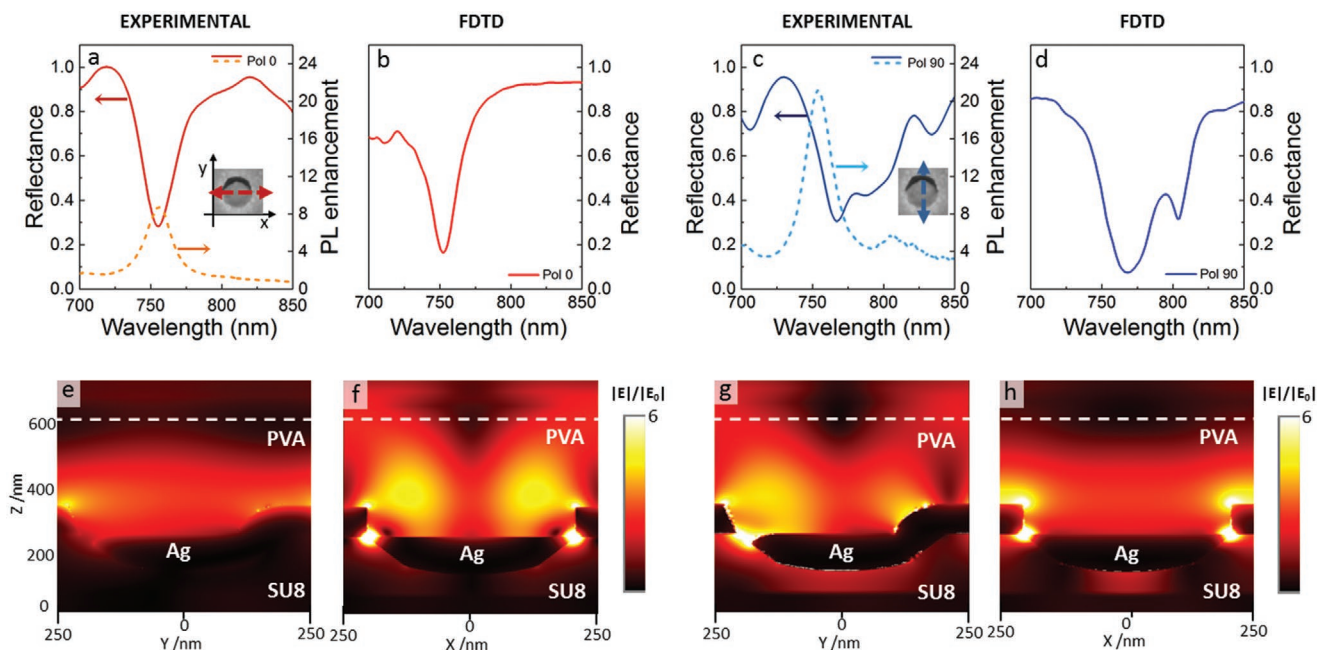


Figure 7. Reflectance and photoluminescence enhancement observed in a plasmonic crystal with 30 nm gaps. a,c) Reflection (solid) and PL enhancement (dashed) profile for polarization 0° and 90°. b,d) FDTD simulated reflectance for polarizations 0° and 90°. Electric field distribution of light at 750 nm for polarization e,f) parallel and g,h) perpendicular to the nanogaps.

3. Conclusion

We have introduced an innovative technique for the fabrication of large-area plasmonic architectures with low symmetry unit cells conferring the ensemble with exciting optical properties over large areas. The combination of nanoimprinted structures with oblique angle deposition of metals paves the way for the exploitation of polarization-dependent optical properties in a scalable way. Combining these two techniques, we produced metasurfaces with different optical response under linearly polarized light with application as polarization filters and for tunable structural coloring. We demonstrate the simple fabrication of chiral metasurfaces with an intense chiroptical response at visible wavelength comparable to the outcome from nanostructures fabricated through focused ion beam lithography and other more expensive techniques. Furthermore, we established the possibility to form nanogap arrays with homogeneous optical properties over 1 cm² areas capable of producing an averaged 20-fold enhancement of the photoluminescence of an organic dye placed on top. This study paves the way toward the implementation of complex optical properties such as artificial magnetism at visible frequencies, optical chirality, and negative refractive index into real applications.

4. Experimental Section

Materials: Prepatterned silicon masters were purchased from Naitec (Navarra, Spain). A hard PDMS silicone elastomer kit was purchased from Gelest (Morrisville, PA) and a soft PDMS Sylgard184 silicone elastomer kit from Dow Corning Corporation (Auburn, MI). 1H,1H,2H,2H-Perfluorooctyltrichlorosilane (PFOTS, 97%) was purchased from Alfa Aesar (Thermo Fisher GmbH, Karlsruhe, Germany). Poly(vinyl alcohol) (Mw 89 000–98 000, 99+% hydrolyzed) was purchased

from Sigma-Aldrich. Atto 655 fluorophores were purchased from Sigma-Aldrich.

Composite Polydimethylsiloxane Molds Fabrication: PDMS molds were fabricated following a previously reported protocol.^[40] Briefly, silicon masters were functionalized with PFOTS as an antisticking layer, lowering the surface energy and allowing the easy release of cured PDMS. The molds were fabricated by casting a thin layer of hard-PDMS on the master followed by a thick layer of soft PDMS as support. The 1 cm² patterns used in this work consist of square arrays of cylindrical pillars with 300 nm diameter, 350 nm height, and lattice parameters of 400, 500, and 600 nm.

Nanoimprinted Films: 2D photonic crystals were fabricated on SU8 2000.5 (Microchem) by nanoimprint lithography using patterned (PDMS) molds. Polished silicon wafer pieces 500 μm thick or glass microslides were used as substrates. The SU8 photoresist was spin-coated to achieve a layer thickness about 650–700 nm. The imprinting process was performed using a CNI NIL nanoimprinting tool at a temperature of 90 °C and a pressure of 2 bars. The samples were UV-cured for 5 min under 365 nm LED light followed by 30 min annealing on a hot plate at 150 °C. The samples were mounted on a standard holder specifically modified to have three different tilt angles (0°, 20°, and 45°) followed by Ag thermal evaporation at 7 × 10⁻⁷ mbar at 1 nm s⁻¹.

Fabrication of Nanostructures with Different Feature Depth: 2D photonic crystals with different depths were fabricated replicating nanostructured silicon wafers with different depths. Briefly, the SU8 2000.5 (Microchem) photoresist was spin-coated to achieve a layer thickness about 350–400 nm and imprinted using a hot embossing technique described in previous reports.^[41] Later, a two-step reactive ion etching (RIE) process was used to transfer the pattern to the silicon substrate: First, a O₂ descumming treatment was used to etch the residual 50–100 nm layer of resist under the imprinted holes (O₂ 40 sccm, pressure 25 mTorr, RIE power 50 W, ICP power 1500 W, and etching rate ≈800 nm min⁻¹); second, the exposed Si was etched with CHF₃ and SF₆ (CHF₃ 50 sccm, SF₆ 15 sccm, pressure 12 mTorr, RIE power 150 W, ICP power 0 W, and etching rate 60 nm min⁻¹). The Si processing time was varied to achieve new silicon masters with hole depths of 120, 80, and 60 nm. A final descumming step was used to

remove entirely the remains of resist. The new masters were replicated in PDMS as described previously and yielded nanostructures with 120, 80, and 60 nm feature depth.

Far-Field Reflection Measurements: An FTIR spectrophotometer attached to an optical microscope (Vertex 70 and Hyperion, Bruker) including a linear polarizer was used to obtain the far-field reflection measurements in the 400–850 nm range. Reflected light was collected through a 4×0.1 NA objective with a spot size of $900\times 900\ \mu\text{m}^2$. The background reflection spectrum was normalized to a silver mirror (96% reflectivity) for both polarizations.

Circular Dichroism Measurements: CD spectra were measured, using a home-built setup. A tungsten halogen lamp (Ocean Optics, HL-2000-HP) was used as light source, the unpolarized light passes through a Glan-Thompson linear polarizer, followed by an achromatic quarter-wave plate (Thorlabs, AQWP05M-600, 400–800 nm), in order to obtain circular polarized light (CPL). Then, the CPL was focused to the sample using low NA lens. The transmitted light was then collected using a fiber coupled spectrophotometer (Ocean Optics, QEPro-FL). The transmittance difference between right and left circular polarized light, $\Delta T = T_{\text{RCP}} - T_{\text{LCP}}$, was used to measure the samples CD.

The nonideal behavior of the optical elements in the measurement setup may degrade the polarization state of the CPL introducing anomalous ellipticity and leading to false CD response (even in achiral structures). In order to prevent this issue, the polarization polar plots were measured, by adding a monitor after the sample focal lens and combining the measurements of 12 different polarization directions. This optimization procedure gives right angle (β) between the linear polarizer and the QWP fast axis (ideally considered as $\pm 45^\circ$) that minimizes their eccentricity for a certain wavelength. Sweeping β , the instrumental calibration function ($\beta(\lambda)$) between the angle and the wavelength that allow to optimize the quality of the CPL in the whole measured spectrum was identified.

Scanning Electron Microscopy (SEM): SEM images were obtained using a Quanta FEI 200 FEG-ESEM microscope operating at 10 kV, and secondary and backscattered electrons were detected in a high-vacuum regime (10^{-3} Pa).

Photoluminescence Measurements: Photoluminescence at ambient conditions was collected in backscattering geometry using a WITec Alpha300 R confocal setup. For excitation, a He–Ne gas laser (633 nm) was coupled into a Zeiss microscope through a wavelength-specific single-mode fiber and collimated by an achromatic lens. The beam was focused onto the sample, with power 0.25 mW, 4×0.1 NA objective, giving an estimated spot size diameter of 7 μm . The pixel size for the images was $50\times 50\ \mu\text{m}^2$, given by the scanning movement of a stepper-motor-driven sample stage. The collected light was focused into a multimode optical fiber, which served as the entrance slit for the spectrometer. The 3.5- μm -diameter single-mode input fiber and the 50- μm -diameter multimode output fiber provided the optical apertures for the confocal arrangement. A Si back-illuminated 1024×127 pixel CCD cooled at -60°C was used for detection. Using gratings of 600 or 300 grooves mm^{-1} the emission spectra were acquired at each image pixel using integration times of 0.1 s. Images were analyzed using WITec Project FOUR software.

Numerical Simulations: FDTD numerical simulations were carried out by means of a commercial software (www.lumerical.com) with a mesh smaller than 3 nm and following the geometrical parameters from the experimental microscopy images for both linear polarizations. Constant refractive indexes of PVA and SU8 were taken as $n = 1.5$ and $n = 1.58$, respectively, and for silver a dispersive Drude model was used where the permittivity of the silver ϵ_{Ag} is

$$\epsilon_{\text{Ag}}(\omega) = 1 - \frac{\omega_{\text{p}}^2}{\omega(i\nu_{\text{c}} + \omega)} \quad (1)$$

where the plasma resonance is set as $\omega_{\text{p}} = 1.37\times 10^{16}$ rad s^{-1} and the plasma collision is $\nu_{\text{c}} = 8.5\times 10^{13}$ rad s^{-1} .

For the Purcell factor calculation an electric dipole has been situated in the middle of the nanogap for both polarizations inside the PVA zone with a surrounding mesh of 0.3 nm.

Supporting Information

Supporting Information is available from the Wiley Online Library or from the author.

Acknowledgements

The Spanish Ministerio de Economía, Industria y Competitividad (MINECO) is gratefully acknowledged for its support through Grant No. MAT2016-79053-P and through Grant No. SEV-2015-0496 in the framework of the Spanish Severo Ochoa Centre of Excellence program. This project received funding from the European Research Council (ERC) under the European Union's Horizon 2020 research and innovation program (Grant Agreement Nos. 637116, ENLIGHTMENT and 648901, FOREMAT) and the Generalitat de Catalunya program AGAUR 2017-SGR-00488. P.M. acknowledges financial support from an FPI contract (2017) of the MICINN (Spain) cofunded by the ESF. L.A.P. is thankful to the Marie Skłodowska-Curie Actions (H2020-MSCA-IF-2018) for grant agreement No. 839402, PLASMIONICO.

Conflict of Interest

The authors declare no conflict of interest.

Keywords

asymmetry, chirality, enhanced fluorescence, nanoimprinting, plasmonic nanostructures

Received: May 12, 2020

Revised: July 2, 2020

Published online:

- [1] K. A. Willets, R. P. Van Duyne, *Annu. Rev. Phys. Chem.* **2007**, *58*, 267.
- [2] A. Poddubny, I. Iorsh, P. Belov, Y. Kivshar, *Nat. Photonics* **2013**, *7*, 948.
- [3] M. Gómez-Castaño, H. Zheng, J. L. García-Pomar, R. Vallée, A. Mihi, S. Ravaine, *Nanoscale Adv.* **2019**, *1*, 1070.
- [4] E. Lenzi, D. Jimenez de Aberasturi, L. M. Liz-Marzán, *ACS Sens.* **2019**, *4*, 1126.
- [5] H. A. Atwater, A. Polman, *Nat. Mater.* **2010**, *9*, 205.
- [6] S. Baek, P. Molet, M. Choi, M. Biondi, O. Ouellette, J. Fan, S. Hoogland, F. P. García de Arquer, A. Mihi, E. H. Sargent, *Adv. Mater.* **2019**, *31*, 1901745.
- [7] J. L. Garcia-Pomar, M. Nieto-Vesperinas, *New J. Phys.* **2005**, *7*, 160.
- [8] G. Lozano, D. J. Louwers, S. R. K. Rodríguez, S. Murai, O. T. A. Jansen, M. A. Verschuuren, J. Gómez Rivas, *Light: Sci. Appl.* **2013**, *2*, e66.
- [9] V. A. Fedotov, M. Rose, S. L. Prosvirnin, N. Papasimakis, N. I. Zheludev, *Phys. Rev. Lett.* **2007**, *99*, 147401.
- [10] R. Singh, W. Cao, I. Al-Naib, L. Cong, W. Withayachumnankul, W. Zhang, *Appl. Phys. Lett.* **2014**, *105*, 171101.
- [11] N. I. Zheludev, S. L. Prosvirnin, N. Papasimakis, V. A. Fedotov, *Nat. Photonics* **2008**, *2*, 351.
- [12] P. Weis, J. L. Garcia-Pomar, M. Rahm, *Opt. Express* **2014**, *22*, 8473.
- [13] N. Liu, S. Kaiser, H. Giessen, *Adv. Mater.* **2008**, *20*, 4521.
- [14] N. Papasimakis, N. I. Zheludev, *Opt. Photonics News* **2009**, *20*, 22.
- [15] Y. Zhao, A. N. Askarpour, L. Sun, J. Shi, X. Li, A. Alù, *Nat. Commun.* **2017**, *8*, 14180.
- [16] H. E. Lee, H. Y. Ahn, J. Mun, Y. Y. Lee, M. Kim, N. H. Cho, K. Chang, W. S. Kim, J. Rho, K. T. Nam, *Nature* **2018**, *556*, 360.
- [17] X. Zhang, A. V. Whitney, J. Zhao, E. M. Hicks, R. P. Van Duyne, *J. Nanosci. Nanotechnol.* **2006**, *6*, 1920.

- [18] M. Maldovan, E. L. Thomas, *Periodic Materials and Interference Lithography: For Photonics, Phononics and Mechanics*, Wiley-VCH, Weinheim, Germany **2009**.
- [19] V. Malyarchuk, F. Hua, N. H. Mack, V. T. Velasquez, J. O. White, R. G. Nuzzo, J. A. Rogers, *Opt. Express* **2005**, *13*, 5669.
- [20] G. Yoon, K. Kim, D. Huh, H. Lee, J. Rho, *Nat. Commun.* **2020**, *11*, 2268.
- [21] M. Byun, D. Lee, M. Kim, Y. Kim, K. Kim, J. G. Ok, J. Rho, H. Lee, *Sci. Rep.* **2017**, *7*, 46314.
- [22] M. A. Verschuuren, M. W. Knight, M. Megens, A. Polman, *Nanotechnology* **2019**, *30*, 345301.
- [23] A. Kosiorek, W. Kandulski, P. Chudzinski, K. Kempa, M. Giersig, *Nano Lett.* **2004**, *4*, 1359.
- [24] Z. Tang, A. Wei, *ACS Nano* **2012**, *6*, 998.
- [25] M. C. Gwinner, E. Koroknay, L. Fu, P. Patoka, W. Kandulski, M. Giersig, H. Giessen, *Small* **2009**, *5*, 400.
- [26] V. E. Bochenkov, D. S. Sutherland, *Opt. Express* **2018**, *26*, 27101.
- [27] Y. Hou, S. Li, Y. Su, X. Huang, Y. Liu, L. Huang, Y. Yu, F. Gao, Z. Zhang, J. Du, *Langmuir* **2013**, *29*, 867.
- [28] B. Ai, Y. Zhao, *Nanophotonics* **2018**, *8*, 1.
- [29] G. K. Larsen, Y. He, W. Ingram, E. T. Lapaquette, J. Wang, Y. Zhao, *Nanoscale* **2014**, *6*, 9467.
- [30] D. J. Beesley, J. Semple, L. K. Jagadamma, A. Amassian, M. A. McLachlan, T. D. Anthopoulos, J. C. Demello, *Nat. Commun.* **2014**, *5*, 3933.
- [31] C. Zhang, H. Subbaraman, Q. Li, Z. Pan, J. G. Ok, T. Ling, C. J. Chung, X. Zhang, X. Lin, R. T. Chen, L. J. Guo, *J. Mater. Chem. C* **2016**, *4*, 5133.
- [32] L. Liu, F. Wu, D. Xiao, F. Teng, D. Xu, L. Feng, N. Lu, *RSC Adv.* **2017**, *7*, 4759.
- [33] M. Zhang, V. Pacheco-Peña, Y. Yu, W. Chen, N. J. Greybush, A. Stein, N. Engheta, C. B. Murray, C. R. Kagan, *Nano Lett.* **2018**, *18*, 7389.
- [34] A. N. Grigorenko, A. K. Geim, H. F. Gleeson, Y. Zhang, A. A. Firsov, I. Y. Khrushchev, J. Petrovic, *Nature* **2005**, *438*, 335.
- [35] Y. Kim, B. Yeom, O. Arteaga, S. J. Yoo, S. G. Lee, J. G. Kim, N. A. Kotov, *Nat. Mater.* **2016**, *15*, 461.
- [36] T. Liu, L. V. Besteiro, T. Liedl, M. A. Correa-Duarte, Z. Wang, A. O. Govorov, *Nano Lett.* **2019**, *19*, 1395.
- [37] S. Murai, S. Oka, S. I. Azzam, A. V. Kildishev, S. Ishii, K. Tanaka, *Opt. Express* **2019**, *27*, 5083.
- [38] C. Zeng, X. Hu, M. Shi, X. Qiu, Y. Li, J. Xia, *J. Light Technol.* **2016**, *34*, 3283.
- [39] J. J. Baumberg, J. Aizpurua, M. H. Mikkelsen, D. R. Smith, *Nat. Mater.* **2019**, *18*, 668.
- [40] T. W. Odom, J. C. Love, D. B. Wolfe, K. E. Paul, G. M. Whitesides, *Langmuir* **2002**, *18*, 5314.
- [41] A. Espinha, C. Dore, C. Matricardi, M. I. Alonso, A. R. Goñi, A. Mihi, *Nat. Photonics* **2018**, *12*, 343.